communications materials

ARTICLE

https://doi.org/10.1038/s43246-022-00292-w OPEN

Bandgap-independent photoconductive detection in two-dimensional Sb_2Te_3

Wanli Ma[1,2], Tuntan Wu[1,2,3], Niangjuan Yao[1], Wei Zhou[1], Lin Jiang[1], Qinxi Qiu[1,2], Jingbo Li[1,2] & Zhiming Huang[1,2,3,4,5]✉

Broadening the spectral range of photodetectors is vital for photodetection. However, current photoelectric detectors are selective to wavelength, which depends on bandgap, and thermal detectors respond slowly at room temperature. It is challenging to achieve photoconductivity independent of the semiconductor bandgap, which is needed to broaden the spectral range of photodetectors. Here, we use 2D semiconductor Sb_2Te_3 to develop a photodetector with metal-semiconductor-metal structure for multiband response, covering visible, infrared, terahertz and millimeter wavelengths at room temperature. This is achieved by the synergy of the photoconductivity of photo-excited electron-hole pairs above the bandgap, and an electromagnetic-induced well effect below the bandgap. The photodetector achieves a responsivity of 0.6 A W^{-1} at 1550 nm, 515 A W^{-1} at 0.340 THz with a bias of 0.2 V, respectively. The response time is 900 ns, which is short compared to the reported detectors based on 2D materials. In addition, it also exhibits a high polarization extinction ratio of 90. These results suggest that our strategy achieves a photoconductivity independent of the semiconductor bandgap to broaden the spectral range of photodetectors, and could be a strong candidate for multiband photodetection systems.

[1] State Key Laboratory of Infrared Physics, Shanghai Institute of Technical Physics, Chinese Academy of Sciences, 500 Yu Tian Road, Shanghai 200083, P. R. China. [2] University of Chinese Academy of Sciences, 19 Yu Quan Road, Beijing 100049, P. R. China. [3] Hangzhou Institute for Advanced Study, University of Chinese Academy of Sciences, 1 Sub-Lane Xiangshan, Hangzhou 310024, P. R. China. [4] Key Laboratory of Space Active Opto-Electronics Technology, Shanghai Institute of Technical Physics, Chinese Academy of Sciences, 500 Yu Tian Road, Shanghai 200083, P. R. China. [5] Institute of Optoelectronics, Fudan University, 2005 Songhu Road, Shanghai 200438, P. R. China. ✉email: zmhuang@mail.sitp.ac.cn

The conversion of light into electrical signals is the core of photodetection technology. Multiple applications, including optical communications, photography, astronomy, and spectroscopy, have attracted a great deal of attention for multiband photodetection[1–5]. Based on photo-excited electron-hole pairs in semiconductor, visible (VIS) and near-infrared (NIR) light can be effectively detected. On account of their excellent sensitivity and fast response in the VIS and IR bands, photon detectors based on conventional semiconductors Si, HgCdTe, and InGaAs have been widely used[6–9]. However, since photon detectors are selective in wavelength, it is difficult to extend their spectral range to longer waves, such as terahertz (THz) and millimeter wave (MMW) with low photon energy[10]. In general, thermal detectors can accomplish broadband detection, but their response time and sensitivity are inferior to those of room-temperature photon detectors[11,12]. Therefore, it's still a huge challenge to develop multiband photon detectors to cover VIS, IR, THz and MMW.

Nowadays, two-dimensional (2D) materials have extraordinary properties, which provide opportunities and have sparked an interest in the development of optoelectronic devices, including multiband photodetectors[2,13–15]. As the micro-nano technology develops, 2D materials can be designed into novel structures to enhance light absorption and achieve multiband detection. A three-dimensional tubular graphene field-effect transistor was developed and demonstrated room-temperature photodetection from ultraviolet to THz[16]. Developing multi-mechanism coordinated devices is also an efficient method for achieving multiband detection[3,15]. For example, Wang et al. developed a detector with an ultrabroad spectrum response ranging from ultraviolet (375 nm) to long-wavelength infrared (10 μm), by coupling the mechanisms of pyroelectrics, photoconductor and phototransistor effects[15]. Recent research has demonstrated that van der Waals heterojunctions in 2D materials are advantageous for the discovery of novel optoelectronic features, hence enhancing device performance and developing device functionality[17–19]. Heterojunction-based THz photodetection has also been reported[5,20]. However, they demonstrated exceptional performance for VIS and IR detection, but limited for THz and MMW detection.

Consequently, attaining sensitive photoconductivity independent of the semiconductor bandgap in order to widen the spectrum range to THz and MMW bands based on 2D materials at ambient temperature still presents difficulties. Utilizing the anti-symmetric electric field and electromagnetic-induced well (EIW) in an ohmic metal-semiconductor-metal (MSM) structure, a photoconductive process was recently developed to detect photons with energies much below the semiconductor bandgap[21,22]. Sb_2Te_3 is a layered semiconductor with a bandgap of ~0.3 eV[23]. Because of its high mobility and stability, narrow bandgap, great different electron concentration from that of the metal at room temperature[24–28], it is suitable to demonstrate the sensitive photoconductivity and EIW effect in MSM structure. At present, it has been applied to infrared detectors[29–32], but there are virtually no reports in THz photodetection.

In this work, we demonstrate a strategy for fast response and multiband photodetection covering VIS, IR, THz and MMW at room temperature using 2D semiconductor Sb_2Te_3 nanosheets. In the VIS and IR bands, the photoresponse results from photo-excited electron-hole pairs in the Sb_2Te_3 nanosheet. The EIW effect in the MSM structure may explain the THz and MMW responses. In addition, the detector exhibits fast response with a response time of 900 ns and sensitive polarization detection with a high polarization extinction ratio (PER) of 90. Furthermore, the excellent performance of the Sb_2Te_3 detector is further verified by THz imaging experiments. Our strategy achieves a photoconductivity independent of the semiconductor bandgap for broadening the spectral range of photodetectors and developing highly sensitive multiband photodetection.

Results and discussion

Characteristics of Sb_2Te_3 material. Sb_2Te_3 composed of V and VI elements has the rhombohedral crystal structure with the space group D_{3d}^5 (R3m), whose unit cell is composed of a sequence of quintuple layers (QL) of Te-Sb-Te-Sb-Te along the ***c***-axis (Fig. 1a). The coupling between two atomic layers in one QL is strong, but much weaker between two QLs, because of the lower van der Waals bond strength. So, we can mechanically peel off the nanosheets of Sb_2Te_3 crystals. Then we identified Sb_2Te_3 nanosheets by micro-Raman spectroscopy to analyze the quality of the nanosheets. The Raman spectrum (Fig. 1b) shows three characteristic peaks at 69.7, 112.7 and 166.7 cm^{-1}, corresponding to A_{1g}^1, E_g^2, A_{1g}^2 phonon modes, respectively, in agreement with the previous reports[33]. It confirms that we have obtained high-quality Sb_2Te_3 crystals, which is an important guarantee for the preparation of high-performance detectors.

After a series of micro-nano processing technologies such as ultraviolet lithography, dual ion beam technique, lift-off and bonding process, the photodetectors were fabricated over a high resistivity silicon substrate covered with a 300 nm SiO_2 (Supplementary Fig. 1 and **Experimental Section**). The scanning electron microscope (SEM) image in Fig. 1c and the atomic force microscopy (AFM) image in Supplementary Fig. 2 show that the channel length a of the detector is 10 μm, the width w of the photosensitive region is 3 μm, and the thickness d of the Sb_2Te_3 nanosheet is 80 nm. The current-voltage (I-V) characteristic in the range of −0.2 to 0.2 V was measured and shown in Fig. 1d. The detector exhibits excellent ohmic behavior with a resistance of 75 ohms. It facilitates the movement of electrons at two metal-semiconductor interfaces.

Herein, the Sb_2Te_3 nanosheet is p-type semiconductor. The transfer characteristic curve (drain current−gate voltage, $I_{ds} - V_g$) of the Sb_2Te_3 field-effect transistor was obtained by sweeping V_g while keeping the source V_{ds} floating at 0.1 V as shown in Supplementary Fig. 3. It confirms that the Sb_2Te_3 is p-type, suggesting the conductivity depends mainly on holes.

Photodetection in the VIS and IR bands. In order to verify our strategy, we conducted a series of experiments to measure the performance of the detector. The schematic of the structure and response mechanism is shown in Fig. 2a. In the VIS and IR bands, when the energy of the incident photon $h\nu$ exceeds the bandgap E_g of Sb_2Te_3 (~0.3 eV), the electrons in the valence band would be excited into the conduction band to form nonequilibrium electron-hole pairs. Thus, the photon detector exhibits a wavelength-dependent response in the VIS and IR bands. Under the applied electric field, the photo-excited electrons and holes are collected by the anode and cathode electrodes, respectively. To verify the performance of the photodetector in the VIS and IR bands, the dependence of the photoresponse on the bias voltage and incident power was measured by the preamplifier SR 570 and the lock-in amplifier SR830 as shown in Figs. 2b and c. According to the responsivity formula:

$$R_I = \frac{I_{ph}}{P \times A}, \tag{1}$$

where I_{ph} is the photocurrent, and P is the power density, A is the photoactive area of the detector. Therefore, the responsivity of the detector can reach 1.1 A W^{-1} under 635 nm radiation and 0.6 A W^{-1} under 1550 nm radiation with a bias voltage of 0.2 V. The quantum efficiency is the ratio of the number of

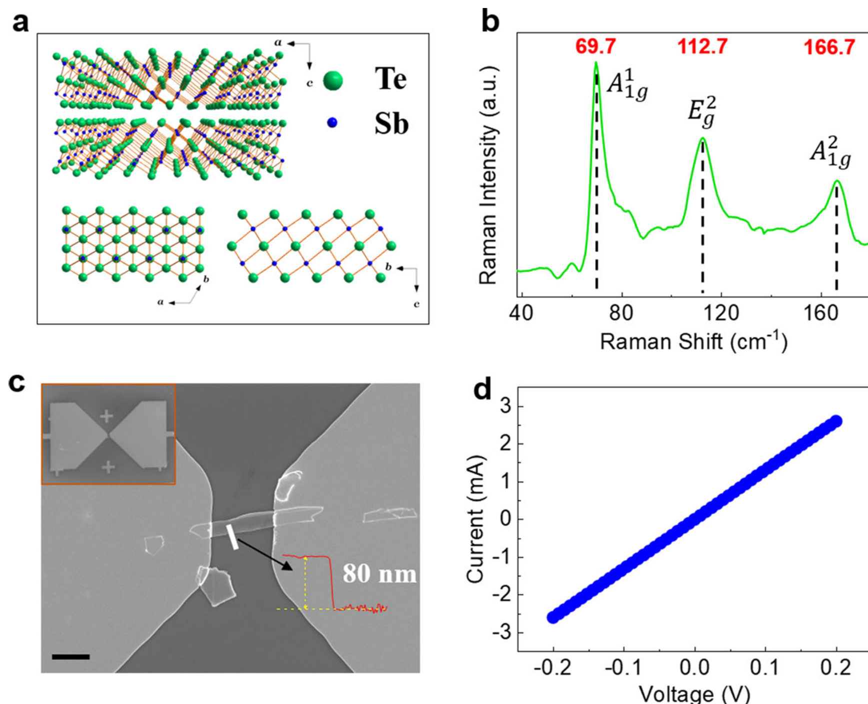

Fig. 1 The characteristics of Sb_2Te_3 material and detector. a Layered crystal structure, the top and side view of the atomic structure of Sb_2Te_3. Green and blue balls denote Te and Sb atoms, respectively. **b** Raman spectrum of Sb_2Te_3. **c** SEM image of detector center. Scale bar, 5 µm. The inset shows the SEM image of the whole detector. Scale bar, 50 µm. **d** Room temperature current-voltage (*I-V*) characteristics of the detector.

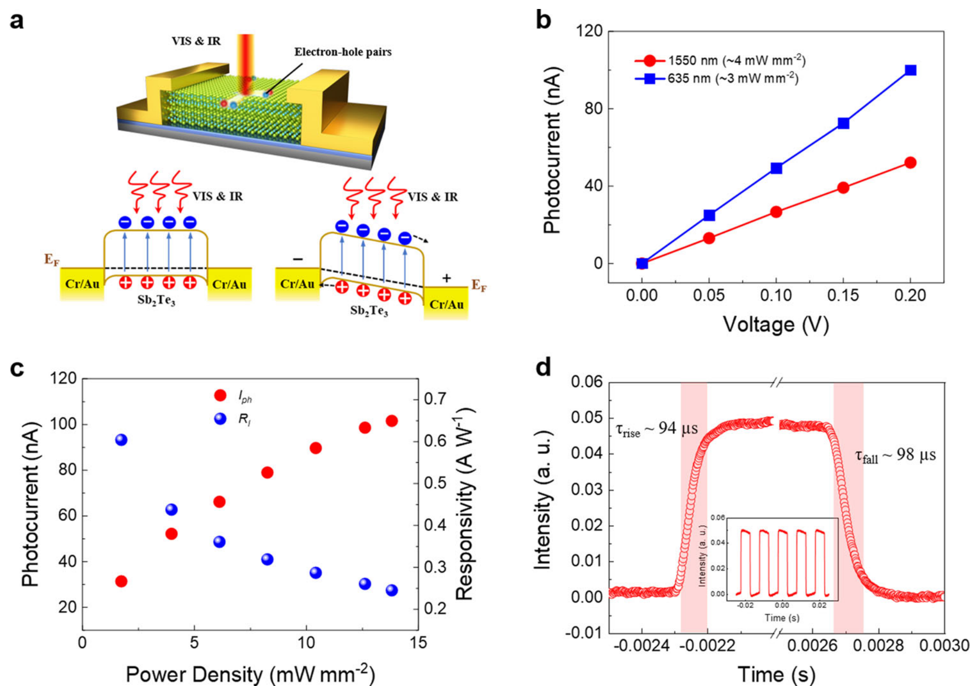

Fig. 2 Response mechanism and performance of the Sb_2Te_3 photodetector in the VIS and IR bands. a Schematic of the structure and response mechanism under VIS and IR radiation. **b** Photocurrent of the photodetector at 635 nm and 1550 nm with different bias voltages. **c** Photocurrent and responsivity of the photodetector as a function of powers with a bias voltage of 0.2 V. **d** Response speed at 635 nm radiation. The inset: the oscillogram under periodic 635 nm radiation.

photoelectrons generated in the photosensitive area to the number of incident photons and can be expressed as:

$$\eta = \frac{N_q}{N_\nu} = \frac{I_{ph}/q}{P \times A/h\nu} = R_I \frac{h\nu}{q}, \quad (2)$$

where N_q is the number of photoelectrons, N_ν is the number of incident photons, q is the elementary charge, ν is the frequency of incident light. Correspondingly, the quantum efficiency is 48.1% under 1550 nm radiation. Meanwhile, the photodetector shows good switching behavior under periodic 635 nm radiation at

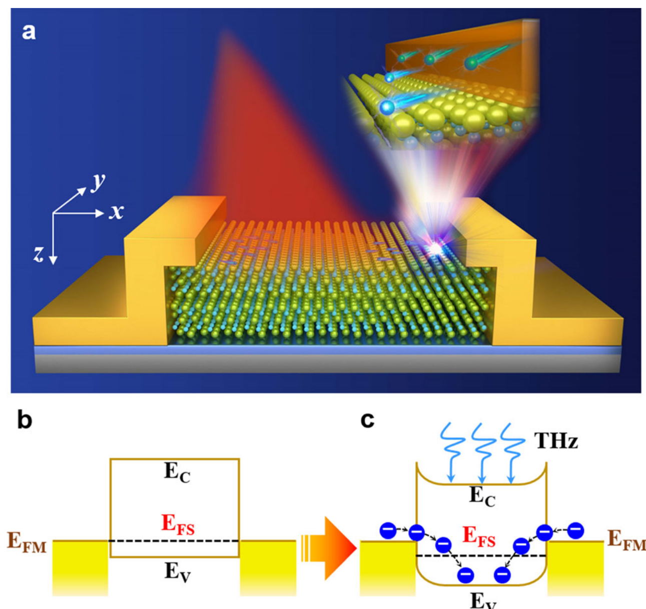

Fig. 3 EIW detection mechanism. a Three-dimensional rendering of the operation principle of the photodetector in the THz band. **b**, **c** Show the band structure of Sb_2Te_3 with MSM structure before and after THz illumination.

room temperature in Fig. 2d. The response time, usually defined as the time measured from 10% up to 90% on the rising edge of photoresponse as well as the recovery time (from 90% down to 10% of the falling edge), is a critical factor of the performance of the detector. Figure 2d shows the response time of the photodetector at 635 nm. The rising and falling times are 94 µs and 98 µs respectively. It can be seen that the Sb_2Te_3 photodetector has outstanding performance in the VIS and NIR bands.

Photodetection in the THz and MMW bands. Generally, when the energy of photons is much smaller than the semiconductor bandgap, photoconductivity based on photo-excited electron-hole pairs cannot be achieved in the semiconductor at room temperature. Herein, while in the THz and MMW bands, EIW effect causes electrons to be generated at room temperature by photons in Sb_2Te_3 well below its bandgap, in the MSM structure with channel length much smaller than the wavelength of the incident light. Figure 3a shows the schematic of the MSM structure and the injection of electrons from the metal to the semiconductor in the photodetector. When the light source is off, the carrier concentration of the metal and semiconductor at the contact area is in a dynamic balance. At this time, the Fermi level of the semiconductor Sb_2Te_3 is closed to the valence band and it is aligned with that of the Cr/Au (Fig. 3b). According to the EIW theory, when the electromagnetic wave is incident on the structure, an electromagnetic-induced well will be generated in the Sb_2Te_3. There are two modes of electric field distribution in semiconductor, symmetric and antisymmetric. However, only the antisymmetric electric field distribution will contribute to the change in the carrier concentration in the semiconductor. The antisymmetric electric field will result in a symmetrical potential distribution. In the one-half period when the antisymmetric electric field appears, the electrons are emitted into the Sb_2Te_3 from two metallic electrodes driven by Lorentz force as shown in Fig. 3c. In the following half period, the injected electrons in the Sb_2Te_3 are decelerated, but further move forward. Therefore, it is equivalent to an electromagnetic-induced well. As a result, the emitted electrons accumulate in the Sb_2Te_3. The Femi level of Sb_2Te_3 decreases and the electrons in the metal are driven to Sb_2Te_3 and trapped by the well (Fig. 3c). Consequently, the conductivity of the Sb_2Te_3 will be changed. With a biased electric field applied, the signal is collected between the two metallic contacts[21,22].

Then, we measured the performance of the photodetector in the THz and MMW bands (0.02–0.04 THz, 0.165–0.172 THz, 0.220–0.330 THz and 0.330–0.346 THz) at room temperature in the atmosphere, with details shown in Supplementary Fig. 4 and Experimental Section. Herein, the photoresponse of our detector was recorded through a lock-in amplifier with a modulation frequency of 1 kHz and a bias of 100 mV as shown in Supplementary Fig. 5. According to EIW theory, the photoresponse depends on the injected electron Δn from the metal in the THz and MMW bands[21,22]. Here, the photocurrent can be expressed as

$$I_{ph} = \frac{\Delta n}{n} \cdot I_b, \tag{3}$$

where I_b is the dark current of the detector (bias current in our case). The photocurrent increases linearly with the increase of the bias voltage at 0.167 THz, 0.270 THz and 0.340 THz in Fig. 4a, which is consistent with Eq. 3 and the EIW theory. According to Eq. 1, the responsivity of the device is 267 A W^{-1} at 0.340 THz, 663 A W^{-1} at 270 THz, 1077 A W^{-1} at 167 THz with a bias voltage of 0.1 V. However, devices based on mechanically exfoliated flakes generally differ in performance. We have fabricated dozens of devices to verify the experimental results. All devices show similar performance as shown in Supplementary Fig. 6, indicating that our strategy is reliable.

According to Eq. 2, the quantum efficiency is 37.6% at 0.340 THz. Since photon energy ($h\nu$) of THz and MMW (~meV) is much smaller than that of VIS and IR (~eV), when the power of the incident light is the same, there will be far more photons of THz and MMW incident on the detector than photons of VIS and IR. Therefore, even though the quantum efficiency in these bands is almost equivalent, the responsivity in the THz band is greater than that in the IR band. The noise equivalent power (NEP) is also a key indicator to estimate the performance of a detector. NEP can be expressed as

$$NEP = \frac{i_n}{R_I}, \tag{4}$$

where i_n is the root mean square (RMS) of the noise current. For our detectors, the main noises considered are the Johnson-Nyquist noise (i_{JN}) and the shot noise (i_{SN}). Thus, the total noise can be described by

$$i_n = \left(i_{JN}{}^2 + i_{SN}{}^2\right)^{0.5} = \left(4k_BT/r + 2qI_d\right)^{0.5}, \tag{5}$$

where k_B is Boltzmann's constant, T is the detector's absolute temperature, r is the resistance of the detector[10]. The NEP of the photodetector is <0.1 pW Hz$^{-0.5}$ with a bias voltage of 0.1 V at 0.340 THz. Moreover, the photoresponse of the detector in the MMW bands has also been verified. According to the EIW theory, the relationship between the injected electron Δn and the power of the incident light can be expressed as $\Delta n = C{\cdot}P$ [21,22], where C is a constant. In addition, combined with Eq. 1, the responsivity is constant as the incident power changes. The photoresponse was measured as the incident power changes with a bias voltage 0.1 V at 0.03 THz. It can be seen from Fig. 4b that the experimental data verifies the Eq. 5. Figure 4b shows that the photocurrent is linear with the incident power range up to 0.5 mW cm^{-2} and the responsivity is nearly constant. Although the power density is <0.01 mW cm^{-2}, the responsivity remains extremely high. To further prove the response of the photodetector, time-resolved measurements were performed at

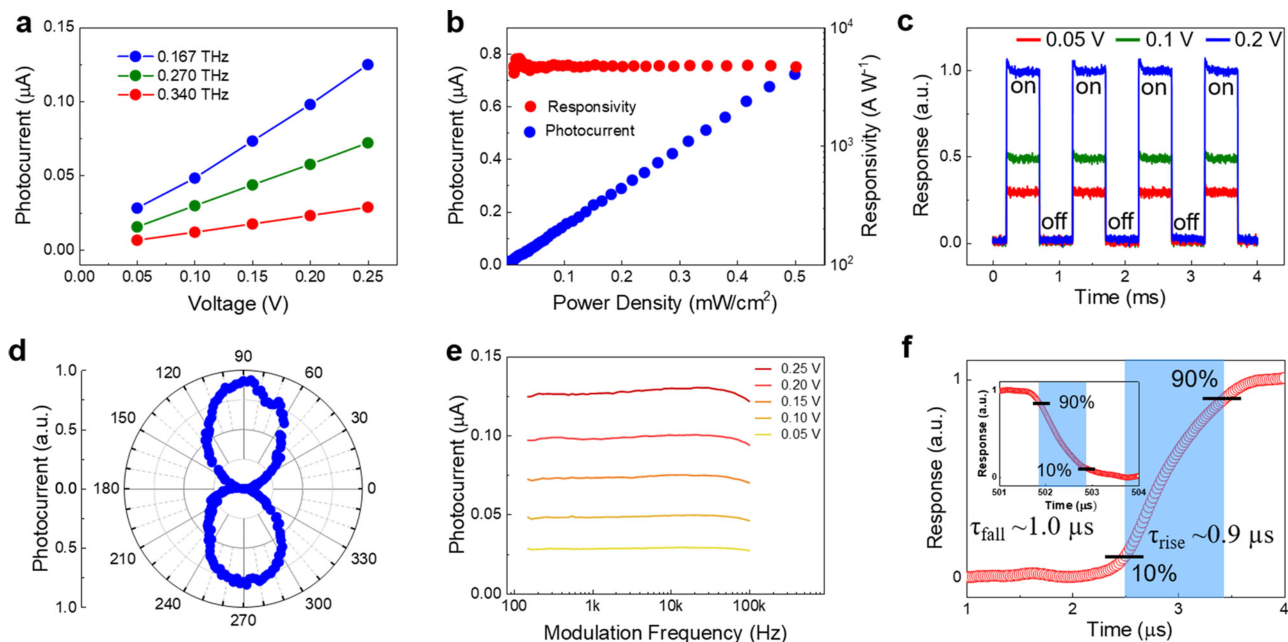

Fig. 4 The performance of the detector in the THz and MMW bands. **a** Photocurrent of the detector under different bias at 0.167 THz, 0.270 THz and 0.340 THz. **b** Dependence of the photocurrent and the responsivity on the radiation intensity at 0.03 THz. **c** Time-resolved measurements at 0.167 THz with different bias voltage of 50 mV, 100 mV and 200 mV. **d** Polarization dependence of the detector at 0.167 THz. **e** Photoresponse of the detector under different bias voltage and modulation frequency. **f** Shows the rising edge and falling edge of the photoresponse in a single time-period.

0.167 THz with bias voltage of 50 mV, 100 mV and 200 mV, as shown in Fig. 4c. In addition to highly sensitive response, polarization detection is another important characteristic of this detector, which is of great significance for revealing unique and multi-dimensional target information[34,35]. As shown in Fig. 4d, the detector is sensitive to the polarization direction of the incident THz. The photocurrent is the largest when the polarization of electromagnetic wave is parallel to the *x*-direction, decreases as the polarization deviates from the *x*-direction, and finally becomes close to zero when the polarization is perpendicular to the *x*-direction. The PER for responsivity is measured to be >90 at 0.167 THz. It is understandable that the MSM structure based on the EIW effect has a strong dependence on the electric-field vector E_x of the electromagnetic wave and antenna gain is directional.

The photocurrent at modulation frequencies 100 Hz to 100 kHz with the bias voltage of 50-250 mV at an interval of 50 mV at 0.167 THz is shown in Fig. 4e, and it had no observable drop even as the modulation frequency increases up to 100 kHz. It means that the Sb_2Te_3 photodetector responds extremely fast. In addition, it was exciting to see that the pulse shape was well preserved even at modulated frequencies from 10 kHz to 100 kHz (Supplementary Fig. 7). The τ_{rise} and τ_{fall} time are determined to be 900 ns and 1 μs, as can be inferred from Fig. 4f, which is fast enough to meet the requirement for fast imaging. It can be seen the same conclusion as in Fig. 4e is that our photodetector has a fast response. In the meantime, it is much faster than the typical room temperature detectors with the response time on the order of milliseconds, such as the Golay cell, pyroelectric detectors[12]. We have compared the performance of the photodetectors based on Sb_2Te_3 and similar semiconductors. As can be seen from Supplementary Table 1, it is difficult to achieve fast response and high responsivity at the same time for Sb_2Te_3 photodetectors in visible and infrared bands. Although our photodetector has a low responsivity, it has a faster response and the response speed is better than most Sb_2Te_3 photodetectors. In the THz band, our detector not only exhibits a fast response, but also has an extremely low NEP, which are superior to most 2D materials THz detectors.

Terahertz imaging. THz wave can penetrate non-metallic and non-polar dielectric such as paper and plastic. Therefore, the THz detection system can detect hidden dangerous weapons and identify illegal drugs to find potential dangers. What's more, compared with *x*-ray technology, THz has no physical harm to the scanned human body[36–38]. To validate the performance of the detector, we performed the scanning imaging experiment and built the imaging system shown in Fig. 5a. The samples are fixed on a 2D translation stage and placed at the focal spot. Then the computer program controls the stage to move the sample in a 2D plane scanning with a step distance of 0.5 mm. The signal detected by the detector is amplified by a preamplifier, read through a lock-in amplifier, and recorded by a computer. Every time the sample moves, the computer records the signal. Each recorded signal intensity is represented by color on the image to form a THz imaging map. Here, a copper coin and a sim card in the envelope as well as a pen were used as objects for imaging. The detector and objects were placed at the THz beam focus, and the THz source was tuned to 0.167 THz. The detector worked at room temperature with a modulation frequency of 1 kHz and a bias voltage of 0.1 V. After optimization, the images are shown in Fig. 5b–d. The shape of the copper coin and the sim card's chip were clearly revealed, even if they were packed in an envelope. In addition, the pen is not completely full of liquid, the quantity of liquid and the air gap inside are clearly checked by the photodetector. The obtained pictures are of high quality, indicating that our detector is promising for fast and large-area imaging.

Conclusion

In summary, we have demonstrated a full photoconductive strategy for broadening the spectral range of photodetectors and developed a high-performance and multiband photodetector with MSM structure covering VIS, IR, THz and MMW at room temperature. The photoresponse is derived from the synergy of

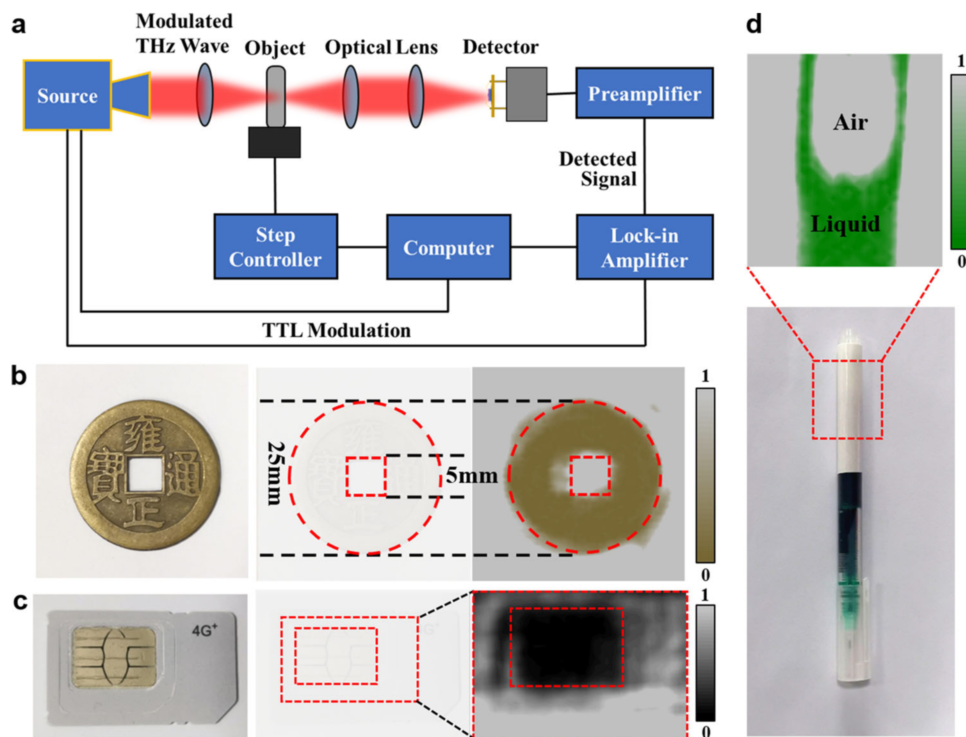

Fig. 5 THz transmission imaging experiments. a Schematic of the setup used for the THz detection and imaging. **b** Photo picture of a copper coin and its THz image. **c** Photo picture of a sim card and its THz image. **d** Photo picture of a pen and THz image of ink capacity of the pen.

photo-excited electron-hole pairs above bandgap in the VIS and IR bands and EIW effect far below bandgap in the THz and MMW bands. In addition, a fast response of 900 ns and a high PER of 90 have been achieved. Finally, THz imaging experiments have demonstrated the excellent performance of the photodetector. The results suggest that our avenue has achieved a photoconductivity independent of the semiconductor bandgap to broaden the spectral range of photodetectors. This strategy is also applicable to other material systems such as doped semiconductors, superlattice materials and heterojunction materials. Our high-performance photodetector will open up a route toward the multiband photodetection system.

Methods

Materials preparation and characterizations. Multilayer Sb_2Te_3 (≈80 nm) was exfoliated onto a substrate of 300 nm SiO_2 over high-resistance silicon ($\rho \approx 10$ kΩ cm) by a blue tape. Raman spectroscopy was measured under a 532 nm laser light using 3 mW power at room temperature. The AFM images and height profiles were acquired by Bruker Dimension Edge. The SEM images were obtained by Raith Nanofabrication-Pioneer Two.

Detector fabrication. The detectors with 20 nm/80 nm thick metal (Cr/Au) contacts were fabricated by ultraviolet lithography, dual ion beam sputtering, lift-off processes and so on. We used UV lithography machine SUSS MJB4, photoresist AZ5214 and developer AZ400 (AZ400K: deionized water = 1:4) to make patterns of electrodes and antennas. The electrodes are made by dual ion beam sputtering technology by Cr and Au with thicknesses of 20 nm and 80 nm respectively. After peeling by acetone, the device was pasted on the base. After bonding process, the detector fabrication was completed.

Photoresponse measurements. For VIS and IR detection, the 635 nm and 1550 nm lasers were used as the source and modulated by a chopper. For THz detection, the electronic frequency multiplication source produced by Virginia Diodes Inc. was used as the source of the THz band, and the frequency coverage was 0.165–0.172 THz and 0.330–0.346 THz. A backward wave tube by Microtech Instruments, Inc. provided radiation in the 0.220–0.330 THz band. In addition, the coverage band of the MMW source (Agilent E8257D) was 0.02–0.04 THz. After the signal detected by the detector was amplified by the preamplifier (SR 570), it was read by the lock-in amplifier (SR 830), which modulated the signal source at the same time. And the data of response time were acquired from a high-speed sampling oscilloscope (Teledyne LeCroy 62Xi-A). Then the detector was replaced by a Golay cell to record the incident power under the exact same measurement conditions. The average power density at 0.167 THz, 0.270 THz and 0.340 THz were about 0.15 mW cm^{-2}, 0.15 mW cm^{-2}, 0.15 mW cm^{-2}, respectively.

Numerical simulations. We also used HFSS to calculate the gain G of the antenna. The maximum gain G of the antenna was about 1.6 at 0.167 THz, 1.8 at 0.270 THz, 2.2 at 0.340 THz as shown in Supplementary Fig. 8.

Data availability

The authors declare that the data that support the graphs within this paper are available from the corresponding author upon reasonable request.

Received: 23 February 2022; Accepted: 14 September 2022;
Published online: 03 October 2022

References

1. Wang, X. et al. Ultrasensitive and broadband MoS(2) photodetector driven by ferroelectrics. *Adv. Mater*. **27**, 6575–6581 (2015).
2. Wang, B. et al. Broadband photodetectors based on 2D group IVA metal chalcogenides semiconductors. *Appl. Mater. Today* **15**, 115–138 (2019).
3. Li, Y. et al. Ultrabroadband, ultraviolet to terahertz, and high sensitivity CH3NH3PbI3 perovskite photodetectors. *Nano Lett.* **20**, 5646–5654 (2020).
4. Wang, B. et al. Present advances and perspectives of broadband photodetectors based on emerging 2D-Xenes beyond graphene. *Nano Res.* **13**, 891–918 (2020).
5. Yao, J., Shao, J., Wang, Y., Zhao, Z. & Yang, G. Ultra-broadband and high response of the Bi2Te3-Si heterojunction and its application as a photodetector at room temperature in harsh working environments. *Nanoscale* **7**, 12535–12541 (2015).
6. Lei, W., Antoszewski, J. & Faraone, L. Progress, challenges, and opportunities for HgCdTe infrared materials and detectors. *Appl. Phys. Rev.* **2**, 041303 (2015).
7. Liu, C. et al. Silicon/2D-material photodetectors: from near-infrared to mid-infrared. *Light Sci. Appl.* **10**, 123 (2021).
8. Zhang, J., Itzler, M. A., Zbinden, H. & Pan, J.-W. Advances in InGaAs/InP single-photon detector systems for quantum communication. *Light Sci. Appl.* **4**, e286 (2015).

9. Rogalski, A. HgCdTe infrared detector material: history, status and outlook. *Rep. Prog. Phys.* **68**, 2267–2336 (2005).
10. Tong, J. et al. Surface plasmon induced direct detection of long wavelength photons. *Nat. Commun.* **8**, 1660 (2017).
11. Martyniuk, P., Antoszewski, J., Martyniuk, M., Faraone, L. & Rogalski, A. New concepts in infrared photodetector designs. *Appl. Phys. Rev.* **1**, 41102 (2014).
12. Rogalski, A. & Piotrowski, J. Intrinsic infrared detectors. *Prog. Quantum. Electron.* **12**, 87–289 (1988).
13. Niu, Y. et al. Ultrabroadband, fast, and flexible photodetector based on HfTe(5)Crystal. *Adv. Opt. Mater.* **8**, 2000833 (2020).
14. Afzal, A. M., Iqbal, M. Z., Dastgeer, G., Ahmad, A. U. & Park, B. Highly sensitive, ultrafast, and broadband photo-detecting field-effect transistor with transition-metal dichalcogenide van der Waals heterostructures of $MoTe_2$ and $PdSe_2$. *Adv. Sci.* https://doi.org/10.1002/advs.202003713 (2021).
15. Wang, X. et al. Multimechanism synergistic photodetectors with ultrabroad spectrum response from 375 nm to 10 microm. *Adv. Sci.* **6**, 1901050 (2019).
16. Deng, T. et al. Three-dimensional graphene field-effect transistors as high-performance photodetectors. *Nano Lett.* **19**, 1494–1503 (2019).
17. Srivastava, P. K. et al. Multifunctional van der Waals broken-gap heterojunction. *Small* **15**, e1804885 (2019).
18. Chen, Y. et al. Ferroelectric-tuned van der Waals heterojunction with band alignment evolution. *Nat. Commun.* **12**, 4030 (2021).
19. Kim, H. et al. Actively variable-spectrum optoelectronics with black phosphorus. *Nature* **596**, 232–237 (2021).
20. Xu, H. et al. PtTe2 -based Type-II dirac semimetal and Its van der Waals heterostructure for sensitive room temperature terahertz photodetection. *Small* **15**, 1903362 (2019).
21. Huang, Z. et al. Room-temperature photoconductivity far below the semiconductor bandgap. *Adv. Mater.* **26**, 6594–6598 (2014).
22. Huang, Z. et al. Extreme sensitivity of room-temperature photoelectric effect for terahertz detection. *Adv. Mater.* **28**, 112–117 (2016).
23. Peranio, N., Eibl, O. & Nurnus, J. Structural and thermoelectric properties of epitaxially grown Bi2Te3 thin films and superlattices. *J. Appl. Phys.* **100**, 114306 (2006).
24. Kim, S. J., We, J. H., Kim, J. S., Kim, G. S. & Cho, B. J. Thermoelectric properties of P-type Sb2Te3 thick film processed by a screen-printing technique and a subsequent annealing process. *J. Alloys Compd.* **582**, 177–180 (2014).
25. Xu, B. et al. Thermoelectric properties of monolayer Sb2Te3. *J. Appl. Phys.* **124**, 165104 (2018).
26. Erdogan, I. Y. & Demir, U. Synthesis and characterization of Sb2Te3 nanofilms via electrochemical co-deposition method. *J. Electroanal. Chem.* **633**, 253–258 (2009).
27. Wang, J. et al. Enhancing thermoelectric performance of Sb2Te3 through swapped bilayer defects. *Nano Energy* **79**, 105484 (2021).
28. Lu, X. et al. Structurally nanocrystalline electrically monocrystalline Sb2Te3 with high thermoelectric performance. *Scr. Mater.* **166**, 81–86 (2019).
29. Zheng, K. et al. Optoelectronic characteristics of a near infrared light photodetector based on a topological insulator Sb2Te3 film. *J. Mater. Chem. C* **3**, 9154–9160 (2015).
30. Pan, X., He, J., Gao, L. & Li, H. Self-filtering monochromatic infrared detectors based on Bi2Se3 (Sb2Te3)/Silicon heterojunctions. *Nanomaterials* **9**, 1771 (2019).
31. Parbatani, A., Song, E. S., Yang, F. & Yu, B. A broadband, self-biased photodiode based on antimony telluride (Sb2Te3) nanocrystals/silicon heterostructures. *Nanoscale* **10**, 15003–15009 (2018).
32. Zhang, Y., Tang, L. & Teng, K. S. High performance broadband photodetectors based on Sb2Te3/n-Si heterostructure. *Nanotechnology* **31**, 304002 (2020).
33. Sosso, G. C., Caravati, S. & Bernasconi, M. Vibrational properties of crystalline Sb2Te3 from first principles. *J. Phys. Condens. Matter* **21**, 095410 (2009).
34. Tong, L. et al. Stable mid-infrared polarization imaging based on quasi-2D tellurium at room temperature. *Nat. Commun.* **11**, 2308 (2020).
35. Yuan, H. et al. Polarization-sensitive broadband photodetector using a black phosphorus vertical p-n junction. *Nat. Nanotechnol.* **10**, 707–713 (2015).
36. Ferguson, B. & Zhang, X. C. Materials for terahertz science and technology. *Nat. Mater.* **1**, 26–33 (2002).
37. Tonouchi, M. Cutting-edge terahertz technology. *Nat. Photon.* **1**, 97–105 (2007).
38. Sizov, F. & Rogalski, A. THz detectors. *Prog. Quantum Electron.* **34**, 278–347 (2010).

Acknowledgements

The authors thanked Yi Shi for kind help. This work was supported by the National Science Funds (Grants No. 12134016, 61625505), Chinese Academy of Sciences (Grants No. ZDBS-LY-JSC025) and Shanghai Municipal Science and Technology Major Project (Grant No.2019SHZDZX01).

Author contributions

Z.H. and W.M. conceived the project. W.M., T.W., and L.J. fabricated the devices. W.M. and N.Y. measured the devices. W.M., T.W., W.Z.,Q.Q., and J.L. analyzed the mechanism of the response. Z.H. and W.M. wrote the manuscript with inputs from all authors.

Competing interests

All authors declare no competing interests.

Additional information

Supplementary information The online version contains supplementary material available at https://doi.org/10.1038/s43246-022-00292-w.

Correspondence and requests for materials should be addressed to Zhiming Huang.

Peer review information *Communications Materials* thanks Changgu Lee and the other, anonymous, reviewer(s) for their contribution to the peer review of this work. Primary Handling Editors: Sunkook Kim and Aldo Isidori. Peer reviewer reports are available.

Reprints and permission information is available at http://www.nature.com/reprints

Publisher's note Springer Nature remains neutral with regard to jurisdictional claims in published maps and institutional affiliations.

Open Access This article is licensed under a Creative Commons Attribution 4.0 International License, which permits use, sharing, adaptation, distribution and reproduction in any medium or format, as long as you give appropriate credit to the original author(s) and the source, provide a link to the Creative Commons license, and indicate if changes were made. The images or other third party material in this article are included in the article's Creative Commons license, unless indicated otherwise in a credit line to the material. If material is not included in the article's Creative Commons license and your intended use is not permitted by statutory regulation or exceeds the permitted use, you will need to obtain permission directly from the copyright holder. To view a copy of this license, visit http://creativecommons.org/licenses/by/4.0/.

© The Author(s) 2022